

# Engineering Dirac Materials: Metamorphic $\text{InAs}_{1-x}\text{Sb}_x/\text{InAs}_{1-y}\text{Sb}_y$ Superlattices with Ultralow Bandgap

Sergey Suchalkin,<sup>\*,†</sup> Gregory Belenky,<sup>†</sup> Maksim Ermolaev,<sup>†</sup> Seongphill Moon,<sup>‡,§</sup> Yuxuan Jiang,<sup>‡,||</sup> David Graf,<sup>‡</sup> Dmitry Smirnov,<sup>‡</sup> Boris Laikhtman,<sup>⊥</sup> Leon Shterengas,<sup>†</sup> Gela Kipshidze,<sup>†</sup> Stefan P. Svensson,<sup>#</sup> and Wendy L. Sarney<sup>#</sup>

<sup>†</sup>State University of New York at Stony Brook, Stony Brook, New York 11794-2350, United States

<sup>‡</sup>National High Magnetic Field Laboratory, Tallahassee, Florida 32310, United States

<sup>§</sup>Department of Physics, Florida State University, Tallahassee, Florida 32306, United States

<sup>||</sup>School of Physics, Georgia Institute of Technology, Atlanta, Georgia 30332, United States

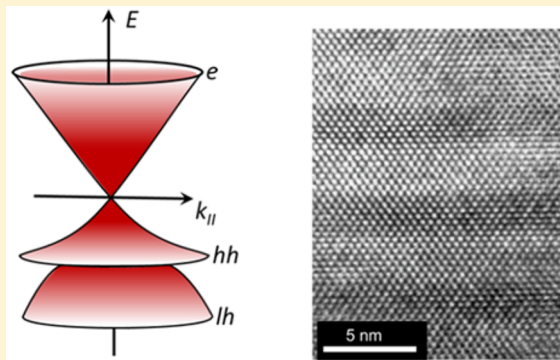
<sup>⊥</sup>Racah Institute of Physics, Hebrew University, Jerusalem 91904, Israel

<sup>#</sup>U.S. Army Research Laboratory, 2800 Powder Mill Road, Adelphi, Maryland 20783, United States

**S** Supporting Information

**ABSTRACT:** Quasiparticles with Dirac-type dispersion can be observed in nearly gapless bulk semiconductor alloys in which the bandgap is controlled through the material composition. We demonstrate that the Dirac dispersion can be realized in short-period  $\text{InAs}_{1-x}\text{Sb}_x/\text{InAs}_{1-y}\text{Sb}_y$  metamorphic superlattices with the bandgap tuned to zero by adjusting the superlattice period and layer strain. The new material has anisotropic carrier dispersion: the carrier energy associated with the in-plane motion is proportional to the wave vector and characterized by the Fermi velocity  $v_F$ , and the dispersion corresponding to the motion in the growth direction is quadratic. Experimental estimate of the Fermi velocity gives  $v_F = 6.7 \times 10^5$  m/s. Remarkably, the Fermi velocity in this system can be controlled by varying the overlap between electron and hole states in the superlattice. Extreme design flexibility makes the short-period metamorphic  $\text{InAs}_{1-x}\text{Sb}_x/\text{InAs}_{1-y}\text{Sb}_y$  superlattice a new prospective platform for studying the effects of charge-carrier chirality and topologically nontrivial states in structures with the inverted bandgaps.

**KEYWORDS:** Dirac materials, metamorphic materials, superlattices, cyclotron resonance



Several materials systems have been found with specific crystal symmetries that produce energy dispersions that deviate from the common quadratic dependence.<sup>1–3</sup> The Dirac Fermion is an example of a solid-state excitation with a dispersion similar to that of a free relativistic particle. In contrast to conventional semiconductors, the dispersions of the electrons and holes in Dirac materials are characterized by the same effective mass, which is directly related to the spectral gap.<sup>4</sup> Dirac Fermions were demonstrated in various materials and systems such as d-wave superconductors,<sup>3</sup> graphene (see ref 3 and the references therein), and narrow-gap semiconductors such as  $\text{HgCdTe}$ ,<sup>5,6</sup>  $\text{Bi}_2\text{Te}_3$ ,<sup>7</sup> and  $\text{ZrTe}_5$ .<sup>8</sup> As the bandgap of a semiconductor material is tuned to zero by alloy composition,<sup>5</sup> temperature,<sup>9</sup> strain,<sup>10,11</sup> or dimensional quantization in semiconductors with an inverted bandgap,<sup>6</sup> strong intermixing of electron and hole states leads to the Dirac-type dispersion.

Another example of semiconductor structure in which zero bandgap can be realized is type II heterostructure with a “broken gap” band alignment in which the effective bandgap is formed by

spatially separated electron and hole states.<sup>12–14</sup> Type II  $\text{InAs}/\text{GaSb}$  composite quantum wells with zero and inverted bandgaps demonstrate a rich phase diagram containing band insulator and quantum spin Hall insulator states.<sup>15–17</sup> The effective bandgap in type II SLs is determined by the thicknesses of the electron and hole containing layers and can be sufficiently different from the bulk bandgaps of the SL layer materials. If the typical width of the SL subbands  $E_S^{\text{SL}}$  in a gapless SL is much larger than the energy scale associated with the in-plane motion  $E_{||}$ ,

$$E_S^{\text{SL}} \gg E_{||} \quad (1)$$

the latter can be considered as a perturbation, and the in-plane energy spectrum is similar to that of the gapless bulk material.<sup>18</sup> This condition can also be expressed as:

**Received:** October 7, 2017

**Revised:** November 27, 2017

**Published:** December 21, 2017

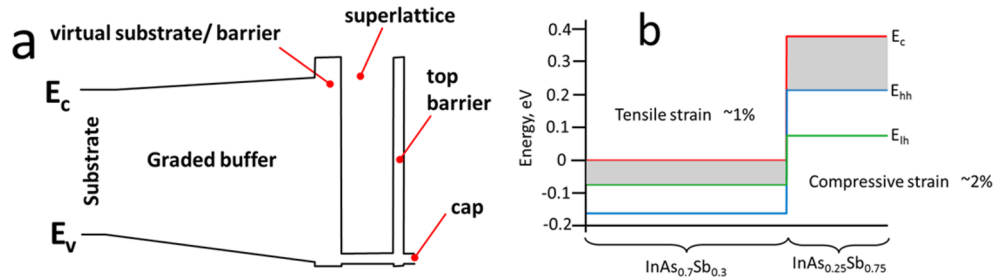


**Figure 1.** Schematic band diagram of (a) the overall structure and (b) bulk-electron ( $E_c$ ), heavy-hole ( $E_{hh}$ ), and light-hole ( $E_{lh}$ ) energies of the SL materials. The gray area corresponds to the bandgap.

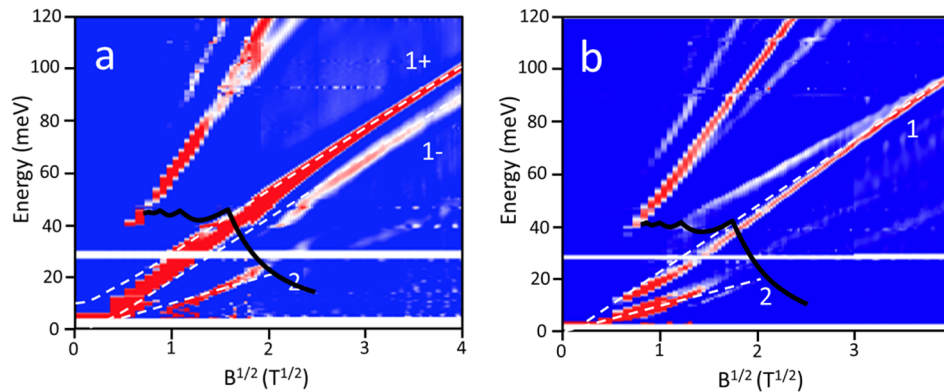


**Figure 2.** Color plot of second derivative of the relative transmission with respect to the frequency  $\frac{d^2}{d\omega^2}(T(B)/T(0))$  as a function of energy and the square root of the magnetic field for the SL with (a) a 6 nm period and (b) the SL with a 7.5 nm period. The red color corresponds to lower magnitudes. Lines 1+, 1-, and 2 represent the transitions between electron LLs. Dashed lines are the transition energies calculated using expression<sup>3</sup>. The solid black line is the calculated dependence of the electron Fermi energy on  $\sqrt{B}$ .

$$k_{\parallel} \ll \frac{\pi}{d} \quad (2)$$

where  $k_{\parallel}$  is the in-plane wave vector and  $d$  is the SL period.<sup>18</sup> A short-period SL with zero bandgap can be realized in an InAsSb system. An InAs<sub>x</sub>Sb<sub>1-x</sub>/InAs<sub>y</sub>Sb<sub>1-y</sub> SLS with  $x > y > 0$  was first proposed by Osborne<sup>19</sup> and experimentally realized by Kurtz et al.,<sup>20</sup> albeit with rather large periods. In contrast to non-common-anion InAs/GaSb SLs, InAs<sub>1-x</sub>Sb<sub>x</sub>/InAs<sub>1-y</sub>Sb<sub>y</sub> SLs<sup>21,22</sup> have common group III elements and can be formed by periodic modulation of group V element composition along the growth axis. Large (~5.9%) lattice constant mismatch between InAs and InSb makes it impossible to grow thick layers of bulk InAsSb alloys or InAs<sub>1-x</sub>Sb<sub>x</sub>/InAs<sub>1-y</sub>Sb<sub>y</sub> SLs using standard InAs or InSb substrates. The virtual substrate approach, developed for an InAsSb system<sup>21,22</sup> allowed continuous variation of the material lattice constant and growing high-quality bulk material in the entire composition range.

Being applied to SLs, the approach allows obtaining thick layers of strain-compensated type-II SLs in which the strain magnitude in electron- and hole-containing layers can be varied independently. This opens the way to fabrication of a new class of semiconductor materials with rich diversity of the electronic properties. An example is ordered InAsSb alloy, which has recently attracted attention as a new potential platform for observing topologically nontrivial phases and realizing Majorana zero modes.<sup>23,24</sup> Reaching zero effective bandgap in a short period, InAs<sub>1-x</sub>Sb<sub>x</sub>/InAs<sub>1-y</sub>Sb<sub>y</sub> SL is made possible by the relative positions and the small (<0.2 eV) bulk bandgaps of the constituents of the SL. In addition, strain of opposite signs applied to electron- and hole-containing layers can further

increase type II band discontinuity and reduce the effective SL bandgap.

In this paper, we demonstrate experimentally that Dirac-type carrier dispersion can be realized in a III-V semiconductor system using a type II InAs<sub>1-x</sub>Sb<sub>x</sub>/InAs<sub>1-y</sub>Sb<sub>y</sub> SL with an effective bandgap close to zero. Interband magneto-absorption and cyclotron resonance were used to probe the electron dispersion for both the in-plane (Faraday geometry) and the growth (Voigt geometry) directions.

A schematic band diagram of the structure is presented in Figure 1. The SL layer is sandwiched between two wide bandgap barriers. The in-plane lattice constant of the structure is ~6.25Å. A pair of samples with 6 nm (structure 1) and 7.5 nm (structure 2) periods were made. The magnetic-field dependence of the cyclotron resonance energy measured in the Faraday geometry is presented in Figure 2. To improve the contrast, we used the second derivative of the relative transmission with respect to the frequency  $\frac{d^2}{d\omega^2}(T(B)/T(0))$  to locate the multiple peak positions. The dependence of the cyclotron resonance (CR) peak energy on  $\sqrt{B}$  is linear in the entire range of the magnetic field. There is a ~10 meV splitting of the CR line observed in structure 1 (Figure 2a). The splitting energy does not depend on the magnetic field. To explain qualitatively the experimental results, we used a simple analytical model of two band envelope wave function.<sup>18,25</sup> According to this model, the in-plane SL energy spectrum near  $k_{\parallel} = 0$  is similar to this of a Dirac Fermion with the rest energy of  $E_g/2$  and Fermi velocity  $v_F$ . The latter is determined by the structure parameters.<sup>18</sup> The LL energies of electrons and heavy holes can be approximated as:

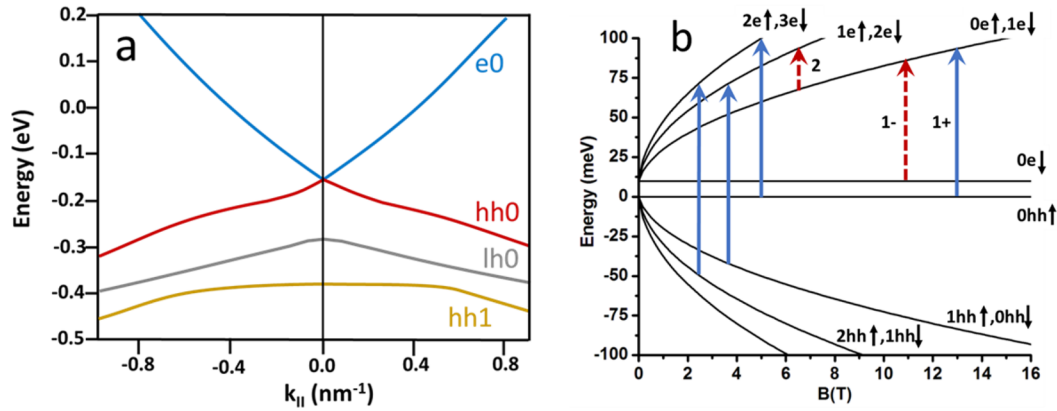


**Figure 3.** In-plane dispersion of the SL with a period of 7.5 nm calculated using 8-band  $k \times p$  method. Zero energy corresponds to the top of the valence band of bulk InSb (panel a); Landau level energies calculated using expression (panels a and b) and the interband (solid arrows) and intraband (dashed arrows) optical transitions (panel b).

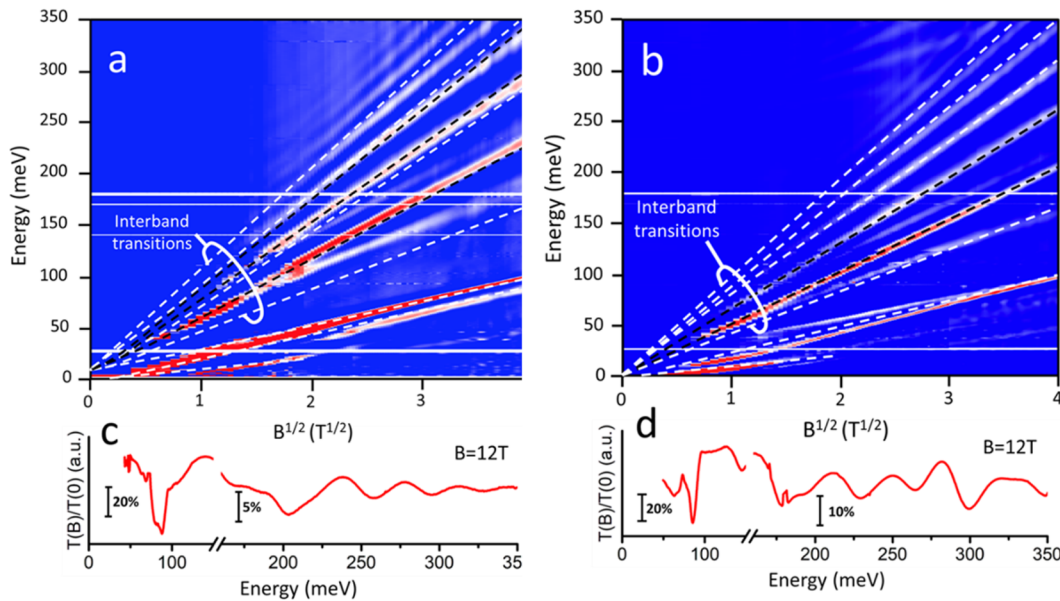


**Figure 4.** Color plot of second derivative of the relative transmission with respect to the frequency  $\frac{d^2}{d\omega^2}(T(B)/T(0))$  as a function of energy and the square root of the magnetic field  $B$  for the SL with (a) a 6 nm period and (b) the SL with a 7.5 nm period. The red color corresponds to lower magnitude. The dashed lines are the calculated transition energies. Samples of the relative transmission spectra for the SL with a (c) 6 nm period and (d) 7.5 nm period.

$$E_{n,e\uparrow} \approx \frac{E_g}{2} + \sqrt{\frac{E_g^2}{4} + \frac{2\hbar^2 v_F^2}{l_B^2}(n+1)}$$

$$E_{n,e\downarrow} \approx \frac{E_g}{2} + \sqrt{\frac{E_g^2}{4} + \frac{2\hbar^2 v_F^2}{l_B^2}n} \tag{3a}$$

$$E_{n,hh\uparrow} \approx \frac{E_g}{2} - \sqrt{\frac{E_g^2}{4} + \frac{2\hbar^2 v_F^2}{l_B^2}n}$$

$$E_{n,hh\downarrow} \approx \frac{E_g}{2} - \sqrt{\frac{E_g^2}{4} + \frac{2\hbar^2 v_F^2}{l_B^2}(n+1)} \tag{3b}$$

Here,  $v_F$  is the Fermi velocity,  $E_g$  for structure 1 is taken as 10 meV,  $E_g$  for structure 2 is zero,  $l_B = \sqrt{\frac{\hbar c}{eB}}$  is the magnetic length and  $\uparrow$  and  $\downarrow$  correspond to different spin projection to the

direction of the magnetic field. For simplicity, the Zeeman splitting is neglected. The selection rules for the optical transitions are  $\Delta n = \pm 1$  for the intraband transitions and  $\Delta n = 0$  and  $\Delta n = \pm 2$  for the interband ones. A transition with  $\Delta n = \pm 2$  occurs due to mixture of conduction and heavy hole bands in strong magnetic field and disappears in the limit of weak magnetic field (see the Supporting Information).

We attributed the CR line  $1^-$  in Figure 2a to the cyclotron resonance (CR) transitions between the ground  $0e \downarrow$  and first  $1e \downarrow$  electron Landau levels (LLs)<sup>6</sup> (Figure 3b). Line  $1+$  corresponds to the transition between zero heavy-hole LL  $0hh \uparrow$  and zero-electron LL  $0e \uparrow$ .

The splitting between the  $1+$  and  $1^-$  transitions is equal to the SL bandgap.<sup>6</sup> Line 2 is the calculated transition energy between  $0e \uparrow, 1e \downarrow$  and  $1e \uparrow, 2e \downarrow$  electron LLs (Figure 3b). This transition is clearly seen at magnetic fields below  $\sim 2$ T. At higher magnetic fields, the LL2 is depleted due to increasing LL degeneracy and the CR transition occurs between the zeroth and first electron

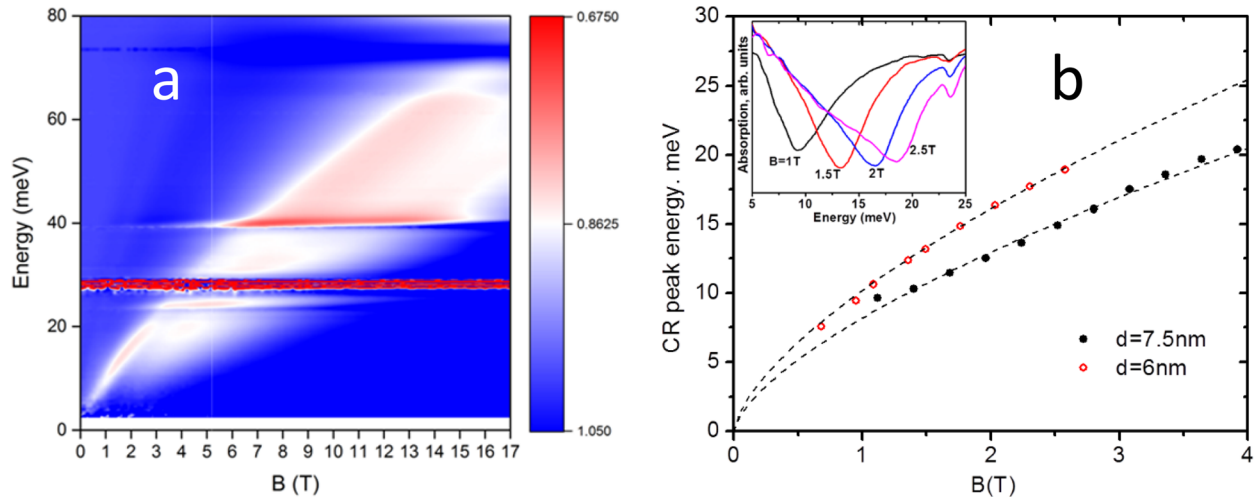


**Figure 5.** Color plot of relative transmission  $T(B)/T(0)$  as a function of energy and magnetic field, parallel to the SL layers, for the SL with a period of (a) 6 nm and (b) magnetic-field dependence of the CR energy. Points are the experimental values, and dashed lines are the CR energies calculated using eq 7. Inset: CR lines at different magnetic fields.

LLs. Experimental CR and electron–hole transition energies follow a  $\sqrt{B}$  dependence for both samples, which indicates linear electron dispersion. The best fit of the experimental dependencies of CR energy on  $\sqrt{B}$  is obtained at  $v_F = 6.7 \cdot 10^5 \frac{m}{s}$  (Figure 2). No splitting of the CR was observed in structure 2, so  $E_g \approx 0$  was assumed. The  $\sqrt{B}$  dependence of the CR energy in this sample corresponds to the same  $v_F$ . The results are qualitatively similar to those observed in nearly gapless HgCdTe.<sup>5,6</sup> The experimental value of  $v_F = 6.7 \cdot 10^5 \frac{m}{s}$  is close to theoretical value,  $v_F = 9 \cdot 10^5 \frac{m}{s}$  obtained from 8-band  $\mathbf{k} \times \mathbf{p}$  calculations<sup>26</sup> (Figure 3a).

Interband optical transitions between electron and hole LLs are observed at higher energies. A color plot of the second derivative of the relative transmission  $T(B)/T(0)$  with respect to the frequency is shown in Figure 4.

Qualitatively, the dependencies of the interband transition energies on the magnetic field are similar in both structures, but the slopes of the corresponding transition energies as functions of  $\sqrt{B}$  is lower in sample 2. This can be explained by the asymmetry between electron and heavy hole dispersion branches at higher energies due to interaction between heavy-hole and light-hole sub-band (Figure 3a). This interaction is stronger in the structure 2 because the energy separation between light- and heavy-hole sub-bands is less in this structure. At energies exceeding  $\sim 100$  meV, the slope of the heavy-hole dispersion becomes lower. In a rough approximation, this effect can be taken into account by introducing different Fermi velocities for electrons and holes. The fitting of the interband transitions for structure 2 is done using electron  $v_F = 6.7 \cdot 10^5 \frac{m}{s}$  and heavy-hole  $v_F = 3.3 \cdot 10^5 \frac{m}{s}$ . The detailed description of the transition energies versus the magnetic field with a more sophisticated model will be presented elsewhere. One of the striking features of the magneto-absorption spectra is that the CR transition energies demonstrate  $\sqrt{B}$  dependence for the entire observed energy range. This dependence is observable at energies that are considerably less than the bandgaps of both ternary alloys of the SL layers (Figure 2). These are  $\sim 100$  meV for 1% tensile strained  $\text{InAs}_{0.7}\text{Sb}_{0.3}$  and  $\sim 200$  meV for 2%

compressively strained  $\text{InAs}_{0.25}\text{Sb}_{0.75}$ . This is an indication that the energy range corresponding to the parabolic region in the in-plane energy spectrum of a short period type II superlattice is determined by the effective SL bandgap rather than the bulk bandgaps of the corresponding SL materials. Because the effective bandgap of the SL is close to zero, the in-plane energy spectrum near  $k_{\parallel} = 0$  is Dirac-type and consists of two symmetrical branches of electrons and heavy holes.

The Fermi velocity in a short-period  $\text{InAs}_{0.7}\text{Sb}_{0.3}/\text{InAs}_{0.25}\text{Sb}_{0.75}$  SL can be calculated as  $v_F = \frac{P_{\text{hh,e}} d}{\sqrt{2} m_0}$ , where  $m_0$  is the free electron mass and  $P_{\text{hh,e}}$  is the averaged over the SL period momentum matrix element between electron and heavy-hole sub-bands<sup>18</sup> (see also eq 9 in the Supporting Information):

$$P_{\text{hh,e}} = P_1 \int_0^{d_1} \xi_e(z) \xi_{\text{hh}}^*(z) dz + P_2 \int_{d_1}^d \xi_e(z) \xi_{\text{hh}}^*(z) dz \quad (4)$$

Here,  $P_1$  and  $P_2$  are the momentum matrix elements between the electron and heavy-hole sub-bands in  $\text{InAs}_{0.7}\text{Sb}_{0.3}$  and  $\text{InAs}_{0.25}\text{Sb}_{0.75}$ ;  $d_1$  is the thickness of the  $\text{InAs}_{0.7}\text{Sb}_{0.3}$  layer; and  $\xi_e(z)$  and  $\xi_{\text{hh}}(z)$  are Kronig–Penney envelope functions for electrons and heavy holes corresponding to the motion in the growth direction. The magnitude  $2P_1^2/m_0$  is  $\sim 19$  eV for  $\text{InAs}$  and 20.5 eV for  $\text{InSb}$ .<sup>27</sup> Taking  $P_1 \approx P_2 \equiv P$ , one obtains:

$$v_F \approx \frac{P}{\sqrt{2} m_0} I \approx 1.2 \cdot 10^6 \cdot I \left[ \frac{m}{s} \right] \quad (5)$$

where  $I \equiv \left| \int_0^d \xi_e(z) \xi_{\text{hh}}^*(z) dz \right|$  is the overlap between electron and heavy-hole states in the SL. A comparison of theoretical expression for  $v_F$ , eq 5, with the experimentally obtained equation  $v_F = 6.7 \cdot 10^5 \frac{m}{s}$  gives  $I = 0.56$ . This is a reasonable value considering that the holes are mostly confined within the  $\text{InAs}_{0.25}\text{Sb}_{0.75}$  layers. Adjusting the design parameters of the metamorphic SLs makes it possible to vary the electron–hole overlap while keeping the effective  $E_g$  of the SL close to zero. As it follows from eq 5, this gives an effective tool with which to control the Fermi velocity.

The interband transitions are not observable at energies less than 40 meV, probably due to the effect of band filling. The carrier concentration obtained from the hall measurements gives  $N \approx 10^{16} \text{ cm}^{-3}$  for the SL with a 6 nm period and  $N \approx 1.7 \times 10^{16}$

$\text{cm}^{-3}$  for the SL with 7.5 nm period. Assuming that the dispersion along the growth direction is parabolic and characterized by the effective mass  $m_{\perp}$ , and the in-plane dispersion is linear and characterized by the Fermi velocity  $v_F$ , the Fermi energy  $E_F$  can be expressed through the carrier density  $N$  as

$$E_F = \left( \frac{15\pi^2 \hbar^3 v_F^2}{4\sqrt{2} \sqrt{m_{\perp}}} N \right)^{2/5} \quad (6)$$

The estimations of the Fermi energy give 25 meV for the 6 nm SL and 30 meV for the 7.5 nm SL. As one can see from Figure 2b, the switch from the LL0–LL1 CR (line 1) transition to LL1–LL2 (line 2) occurs at a CR energy of  $\sim 30$  meV. The sum of the Fermi energy and the effective SL bandgap gives the lowest energy at which the interband optical transitions can be observed. Calculated dependence of the electron Fermi energy on  $\sqrt{B}$  is shown as the solid black line in Figures 2 a,b. The dependence  $E_F(\sqrt{B})$  was obtained in the limit of a strong magnetic field from the following expression:

$$\int_0^{E_F} d\varepsilon \frac{\sqrt{2m_{\perp}}}{4\pi\hbar l_B^2} \sum_{n,\uparrow,\downarrow} \frac{\Theta(\varepsilon - E_{n,e\uparrow\downarrow})}{\sqrt{\varepsilon - E_{n,e\uparrow\downarrow}}} = N \quad (7)$$

where  $\Theta(x)$  is the step function,  $E_{n,e\uparrow\downarrow}$  are LL energies determined from eqs 3a, and  $m_{\perp}$  is obtained from magneto-absorption measurements in Voigt geometry, as described later. We neglected the LL broadening and assumed that the electron concentration does not depend on the magnetic field.

A color plot of the far-infrared magneto absorption for the magnetic field, parallel to the SL layer (Voigt geometry), is shown in Figure 5a. The magnetic field in the Voigt geometry mixes the in-plane and vertical motion of the carriers. It follows from the Kronig–Penney model that at vertical wave vectors,  $k_{\perp} \ll \frac{\pi}{d}$ , the carrier dispersion in the SL growth direction is parabolic and can be characterized by an effective mass  $m_{\perp}$ . This leads to a sufficiently different dependence of the CR energy on the magnetic field compared to the Faraday geometry. A clear CR peak is observed for magnetic fields below 4 T (Figure 5b, inset). The peak broadens at higher magnetic fields. This can be attributed to the onset of interface-bound CR,<sup>28,29</sup> as the magnetic length becomes closer to the SL period. At magnetic fields below 4 T the magnetic length exceeds 12.8 nm, which is larger than the SL periods. If the effective SL bandgap is  $\sim 0$  and  $m_{\perp e} \ll m_{\perp hh}$ , the LL energy  $E$  can be written as (see the Supporting Information):

$$E_n^{3/2} = \sqrt{2} v_F \sqrt{m_{\perp e}} \hbar \omega_{\perp e} \left( n + \frac{1}{2} \right), \text{ where } \omega_{\perp e} = \frac{eB}{m_{\perp e} c} \quad (8)$$

The dashed lines in Figure 4b are the CR peak energy calculated using eq 7 with  $m_{\perp} = 0.034m_0$  for the SL with  $d = 6$  nm and  $m_{\perp} = 0.065m_0$  for the SL with  $d = 7.5$  nm.

In conclusion, we have demonstrated experimentally that the in-plane dispersion in ultralow-bandgap metamorphic In-As<sub>1-x</sub>Sb<sub>x</sub>/InAs<sub>1-y</sub>Sb<sub>y</sub> superlattices is Dirac type with the Fermi velocity  $v_F = 6.7 \cdot 10^5 \frac{m}{s}$ . The Fermi velocity is proportional to the overlap of the electron and hole states in the SL, which in our case is  $\sim 0.56$ . It was found that the electron dispersion in the growth direction is parabolic at low energies and can be characterized by an effective mass of  $0.034m_0$  in the SL with a

period of 6 nm and  $0.065m_0$  in the SL with a period of 7.5 nm. Applying the virtual substrate approach makes it possible to control the parameters of the in-plane and vertical carrier electron dispersion while keeping the same value of the effective bandgap.

## METHODS

The growth was done with solid-state molecular beam epitaxy using a VEECO GEN-930 system equipped with As and Sb valved cracker sources. The metamorphic AlGaInSb buffer layers were used to create virtual substrate with lattice constant equal to  $\sim 6.25A$ , corresponding to the ultralow bandgap SL average composition. A 3  $\mu\text{m}$  thick buffer layers had linearly graded chemical composition, changing from GaSb to Al<sub>0.57</sub>In<sub>0.43</sub>Sb. The lattice constant of the followed Al<sub>0.67</sub>In<sub>0.33</sub>Sb virtual substrate were matched to the lattice constant of relaxed top part of graded buffer. The metamorphic buffer and virtual substrate were grown at 440 °C and then reduced to 400 °C for the subsequent growth of SL structure. The 1 ML/s growth rate were used for the growth of each layer. A V-to-III ratio was chosen to be equal to 1.1/1.3.

The structures were grown on unintentionally doped (100) GaSb substrates. A GaSb buffer layer was followed by a 2800 nm graded buffer with the composition varied from GaSb to Al<sub>0.58</sub>In<sub>0.42</sub>Sb. This was terminated with a wide bandgap Al<sub>0.58</sub>In<sub>0.42</sub>Sb virtual substrate and lower barrier with a lattice constant of 6.25 Å.<sup>21</sup> The thickness of the absorber layer, consisting of a InAs<sub>0.7</sub>Sb<sub>0.3</sub>/InAs<sub>0.25</sub>Sb<sub>0.75</sub> SL, is 1  $\mu\text{m}$ . The InAs<sub>0.7</sub>Sb<sub>0.3</sub> layers are under 1% tensile strain, while the InAs<sub>0.25</sub>Sb<sub>0.75</sub> layers are under  $\sim 2\%$  compressive strain. Strain balance was achieved by using a layer thickness ratio of 2. The absorber layer was terminated with a 200 nm Al<sub>0.58</sub>In<sub>0.42</sub>Sb barrier and a 50 nm cap made of the same SL. To avoid the formation of 2D electron pockets at the sample boundaries, the barriers and the cap were p-doped at a concentration of  $10^{16} \text{ cm}^{-3}$ . To measure magneto-absorption, the samples were placed in a liquid He cryostat with a superconductive magnet. Magneto-transport measurements were done on 2.4 mm long and 200  $\mu\text{m}$  wide Hall bars. Ohmic contacts were fabricated by deposition of Ni/Au/Ge/Ni/Au layers and rapid thermal annealing at 250 °C. The cap and top barrier layers were etched down at the contact areas before the contact deposition. The SL band structure was simulated using an eight band  $\mathbf{k} \times \mathbf{p}$  envelope function method implemented into NEXTNANO software (see ref 26 and references therein).

## ASSOCIATED CONTENT

### Supporting Information

The Supporting Information is available free of charge on the ACS Publications website at DOI: 10.1021/acs.nanolett.7b04304.

Additional information on experimental calculations.

(PDF)

## AUTHOR INFORMATION

### Corresponding Author

\*E-mail: sergey.suchalkin@stonybrook.edu.

### Notes

The authors declare no competing financial interest.

## ■ ACKNOWLEDGMENTS

The authors appreciate helpful discussions with A. Abanov. The work is supported by U.S. Army Research Office grant no. W911TA-16-2-0053. S.M., Y.J., and D.S. acknowledge the support from the U.S. Department of Energy (grant no. DE-FG02-07ER46451) for IR magneto-spectroscopy measurements that were performed at the National High Magnetic Field Laboratory, which is supported by National Science Foundation (NSF) Cooperative Agreement no. DMR-1157490 and the State of Florida.

## ■ REFERENCES

- (1) Bradlyn, B.; Cano, J.; Wang, Z. J.; Vergniory, M. G.; Felser, C.; Cava, R. J.; Bernevig, B. A. Beyond Dirac and Weyl fermions: Unconventional quasiparticles in conventional crystals. *Science* **2016**, *353*, 558.
- (2) Zhu, Z. M.; Winkler, G. W.; Wu, Q. S.; Li, J.; Soluyanov, A. A. Triple Point Topological Metals. *Phys. Rev. X* **2016**, *6*, 031003.
- (3) Wehling, T. O.; Black-Schaffer, A. M.; Balatsky, A. V. Dirac materials. *Adv. Phys.* **2014**, *63*, 1–76.
- (4) Zawadzki, W. *Semirelativity in Semiconductors: a Review*. 2017, arXiv:1701.07067v1. arXiv.org e-Print Archive. <https://arxiv.org/pdf/1701.07067.pdf> (accessed).
- (5) Orlita, M.; Basko, D. M.; Zholudev, M. S.; Teppe, F.; Knap, W.; Gavrilenko, V. I.; Mikhailov, N. N.; Dvoretiskii, S. A.; Neugebauer, P.; Faugeras, C.; Barra, A. L.; Martinez, G.; Potemski, M. Observation of three-dimensional massless Kane fermions in a zinc-blende crystal. *Nat. Phys.* **2014**, *10*, 233–238.
- (6) Ludwig, J.; Vasilyev, Y. B.; Mikhailov, N. N.; Poumirol, J. M.; Jiang, Z.; Vafeek, O.; Smirnov, D. Cyclotron resonance of single-valley Dirac fermions in nearly gapless HgTe quantum wells. *Phys. Rev. B: Condens. Matter Mater. Phys.* **2014**, *89*, 241406.
- (7) Orlita, M.; Piot, B. A.; Martinez, G.; Kumar, N. K. S.; Faugeras, C.; Potemski, M.; Michel, C.; Hankiewicz, E. M.; Brauner, T.; Drasar, C.; Schreyeck, S.; Grauer, S.; Brunner, K.; Gould, C.; Brune, C.; Molenkamp, L. W. Magneto-Optics of Massive Dirac Fermions in Bulk Bi<sub>2</sub>Se<sub>3</sub>. *Phys. Rev. Lett.* **2015**, *114*, 185401.
- (8) Li, Q.; Kharzeev, D. E.; Zhang, C.; Huang, Y.; Pletikoscic, I.; Fedorov, A. V.; Zhong, R. D.; Schneeloch, J. A.; Gu, G. D.; Valla, T. Chiral magnetic effect in ZrTe<sub>5</sub>. *Nat. Phys.* **2016**, *12*, 550.
- (9) Teppe, F.; Marcinkiewicz, M.; Krishtopenko, S. S.; Ruffenach, S.; Consejo, C.; Kadykov, A. M.; Desrat, W.; But, D.; Knap, W.; Ludwig, J.; Moon, S.; Smirnov, D.; Orlita, M.; Jiang, Z.; Morozov, S. V.; Gavrilenko, V. I.; Mikhailov, N. N.; Dvoretiskii, S. A. Temperature-driven massless Kane fermions in HgCdTe crystals. *Nat. Commun.* **2016**, *7*, 12576.
- (10) Brune, C.; Liu, C. X.; Novik, E. G.; Hankiewicz, E. M.; Buhmann, H.; Chen, Y. L.; Qi, X. L.; Shen, Z. X.; Zhang, S. C.; Molenkamp, L. W. Quantum Hall Effect from the Topological Surface States of Strained Bulk HgTe. *Phys. Rev. Lett.* **2011**, *106*, 126803.
- (11) Leubner, P.; Lunczer, L.; Brune, C.; Buhmann, H.; Molenkamp, L. W. Strain Engineering of the Band Gap of HgTe Quantum Wells Using Superlattice Virtual Substrates. *Phys. Rev. Lett.* **2016**, *117*, 086403.
- (12) Haddadi, A.; Chen, G.; Chevallier, R.; Hoang, A. M.; Razeghi, M. InAs/InAs<sub>x</sub>Sb<sub>1-x</sub> superlattices for high performance long wavelength infrared detection. *Appl. Phys. Lett.* **2014**, *105*, 121104.
- (13) Lackner, D.; Steger, M.; Thewalt, M. L. W.; Pitts, O. J.; Cherng, Y. T.; Watkins, S. P.; Plis, E.; Krishna, S. InAs/InAsSb strain balanced superlattices for optical detectors: Material properties and energy band simulations. *J. Appl. Phys.* **2012**, *111*, 034507.
- (14) Lackner, D.; Steger, M.; Thewalt, M. L. W.; Pitts, O. J.; Yang, A.; Watkins, S. P. Strain balanced InAs/InAsSb superlattice structures with optical emission to 10 μm. *Appl. Phys. Lett.* **2009**, *95*, 081906.
- (15) Knez, I.; Du, R. R.; Sullivan, G. Evidence for Helical Edge Modes in Inverted InAs/GaSb Quantum Wells. *Phys. Rev. Lett.* **2011**, *107*, 136603.
- (16) Knez, I.; Rettner, C. T.; Yang, S. H.; Parkin, S. S. P.; Du, L. J.; Du, R. R.; Sullivan, G. Observation of Edge Transport in the Disordered Regime of Topologically Insulating InAs/GaSb Quantum Wells. *Phys. Rev. Lett.* **2014**, *112*, 026602.
- (17) Liu, C. X.; Hughes, T. L.; Qi, X. L.; Wang, K.; Zhang, S. C. Quantum spin Hall effect in inverted Type-II semiconductors. *Phys. Rev. Lett.* **2008**, *100* (4), 236601.
- (18) Laikhtman, B.; Suchalkin, S.; Belenky, G. In-plane spectrum in superlattices. *Phys. Rev. B: Condens. Matter Mater. Phys.* **2017**, *95*, 9235401.
- (19) Osbourn, G. C. InAsSb strained-layer superlattices for long wavelength detector applications. *J. Vac. Sci. Technol., B: Microelectron. Process. Phenom.* **1984**, *2*, 176–178.
- (20) Kurtz, S. R.; Dawson, L. R.; Biefeld, R. M.; Follstaedt, D. M.; Doyle, B. L. Ordering induced band-gap reduction in InAs<sub>1-x</sub>Sb<sub>x</sub> alloys and superlattices. *Phys. Rev. B: Condens. Matter Mater. Phys.* **1992**, *46*, 1909–1912.
- (21) Belenky, G.; Donetsky, D.; Kipshidze, G.; Wang, D.; Shterengas, L.; Sarney, W. L.; Svensson, S. P. Properties of unrelaxed InAs<sub>1-x</sub>Sb<sub>x</sub> alloys grown on compositionally graded buffers. *Appl. Phys. Lett.* **2011**, *99*, 141116.
- (22) Belenky, G.; Lin, Y.; Shterengas, L.; Donetsky, D.; Kipshidze, G.; Suchalkin, S. Lattice parameter engineering for III-V long wave infrared photonics. *Electron. Lett.* **2015**, *51*, 1521.
- (23) Winkler, G. W.; Wu, Q. S.; Troyer, M.; Krogstrup, P.; Soluyanov, A. A. Topological Phases in InAs<sub>1-x</sub>Sb<sub>x</sub>: From Novel Topological Semimetal to Majorana Wire. *Phys. Rev. Lett.* **2016**, *117*, 076403.
- (24) Namjoo, S.; Rozatian, A. S. H.; Jabbari, I. Influence of lattice expansion on the topological band order of InAs<sub>x</sub>Sb<sub>1-x</sub> (x = 0, 0.25, 0.5, 0.75, 1) alloys. *J. Alloys Compd.* **2015**, *628*, 458.
- (25) Bernevig, B. A.; Hughes, T. L.; Zhang, S. C. Quantum spin Hall effect and topological phase transition in HgTe quantum wells. *Science* **2006**, *314*, 1757.
- (26) Andlauer, T.; Vogl, P. Full-band envelope-function approach for type-II broken-gap superlattices. *Phys. Rev. B: Condens. Matter Mater. Phys.* **2009**, *80*, 035304.
- (27) Jogai, B.; Talwar, D. N. Interband optical absorption in strained InAs/In<sub>x</sub>Ga<sub>1-x</sub>Sb type-II superlattices. *Phys. Rev. B: Condens. Matter Mater. Phys.* **1996**, *54*, 14524.
- (28) Duffield, T.; Bhat, R.; Koza, M.; Derosa, F.; Hwang, D. M.; Grabbe, P.; Allen, S. J. Electron mass tunneling along the growth direction of (Al,Ga)As/GaAs semiconductor superlattices. *Phys. Rev. Lett.* **1986**, *56*, 2724.
- (29) Duffield, T.; Bhat, R.; Koza, M.; Derosa, F.; Rush, K. M.; Allen, S. J. Barrier-bound resonances in semiconductor superlattices in strong magnetic fields. *Phys. Rev. Lett.* **1987**, *59*, 2693–2696.